OMAE2021-62256

EFFICIENT CALCULATION OF SPATIAL AND TEMPORAL EVOLUTION OF HYDRODYNAMIC LOADS ON OFFSHORE WIND SUBSTRUCTURES

Csaba Pakozdi[*]
SINTEF Ocean, P.O.Box 4762 Sluppen
N-7465 Trondheim, Norway
Phone: +47 45 42 77 83
Email: csaba.pakozdi@sintef.no

**Arun Kamath
Weizhi Wang
Tobias Martin
Hans Bihs**
Dept. of Civil and Env. Eng. NTNU
Trondheim, Norway

ABSTRACT

Estimation of the hydrodynamic loads based on strip theory with the Morrison equation provides a fast and inexpensive method for load estimation for the offshore industry. The advantage of this approach is that it requires only the undisturbed wave kinematics along with inertia and viscous force coefficients. Over the recent years, the development in numerical wave tank simulations makes it possible to simulate nonlinear three-hour sea states, with computational times in the order of real time. This provides an opportunity to calculate loads using wave spectrum input in numerical simulations at reasonable computational time and effort. In the current paper, the open-source fully nonlinear potential flow model REEF3D::FNPF is employed for the wave propagation calculations. Here, the Laplace equation for the velocity potential is solved on a sigma-coordinate mesh with the nonlinear free surface boundary conditions to close the system. A technique to calculate the total acceleration on the sigma-coordinate grid is introduced which makes it possible to apply strip theory in a moving grid framework. With the combination of strip theory and three-hour wave simulations, a unique possibility to estimate the hydrodynamic loads in real time for all discrete positions in space within the domain of the numerical wave tank is presented in this paper. The numerical results for inline forces on an offshore wind mono-pile substructure are compared with measurements, and the new approach shows good agreement.

INTRODUCTION

In the safe and economical design of marine structures, the accurate prediction of the hydrodynamical load is essential [1]. For moderate sea states, theoretical models up to the second order are developed and successfully applied to estimate the hydrodynamical loads for large vessels and platforms in infinite water depth. The limitation of these models is that they are not accurate enough for sea states with steep and breaking waves [2]. In addition, extreme loads can act on the structure during such sea states, which can effect the integrity of the structure or result in large damage. In the past hydrodynamical loads for such sea states were mainly estimated with help of experiments, for the offshore gas and oil industry [3]. Such experiments, which provide detailed information about the hydrodynamical loads on the structure are complicated, expensive and can be properly performed only at a few facilities in the world.

The major developments over the last decades in the hardware and software related to scientific computations provides an alternative to physical modeling, Computational Fluid Dynamics (CFD) which solves the Navier-Stokes equations while representing both phases- water and the air. CFD is successfully applied to estimate loads due to run-up or wave impact events which cannot be calculated with traditional hydrodynam-

[*]Address all correspondence to this author.

ical methods [4, 5]. A large number of publications report CFD simulations where hydrodynamical loads are calculated with very good accuracy when the waves are correctly represented in the simulation [6]. However, for the generation of the correct nonlinear waves, it is necessary to let the waves propagate over a long distance of over 20-30 wavelengths, making the simulation time consuming and computationally expensive. In order to overcome this large demand on resources, one solution is the coupling of potential theory-based numerical wave tanks (NWT) with a two-phase CFD model [7, 8], which is seen as a valid industrial application. The area of application of such NWTs is most meaningful for steep and high sea states, which cannot be described by analytical models such as second order irregular wave models [9, 10]. The appearance of breaking waves in such sea states of three-hours duration is unavoidable. This means that the NWT simulation becomes unstable when breaking waves appear in the simulation, without any strategy to stabilize the potential theory-based model. In a coupled method, the waves propagate a long distance in the NWT and the objective is not to simulate each breaking wave during propagation but to let the potential theory based simulation survive such an event and replicate the energy dissipation due to the wave breaking. Several techniques are presented in the recent years to this effect [7].

In order to provide useful hydrodynamic loads to the more cost sensitive offshore wind and aquaculture industries which have lower safety margins compared to the oil and gas industry, it is necessary to provide cheaper alternatives to physical modeling. Further, fixed mono-pile based wind-platforms are located in finite water depth where the incident waves are steeper than in infinite water depth and the structures are more slender compared to offshore platforms. Due to the above mentioned one-way coupling depending upon a CFD simulation, which is still expensive, this paper investigates the possibility and/or the consequences to estimating the hydrodynamic load acting on mono-piles without the CFD simulation. The Morison equation is generally used in the design of slender structures. If the undisturbed wave kinematics, such as the water particle acceleration and velocity field under waves are known it is possible to achieve good prediction of the hydrodynamical load with empirical force coefficients [11].

The current approach to initial design of offshore structures involves a combination of model tests and second-order wave theory to reconstruct the wave kinematics to determine the wave forces through the Morison equation. This routine becomes difficult to apply to steep waves without model test data, where the second-order theory is not valid. In this article, a novel approach combining a fully nonlinear numerical wave tank (NWT) using the sigma-grid with strip theory and the Morison equation in an Arbitrary Euler-Lagrangian (ALE) framework is presented. This provides improved wave kinematics from the nonlinear numerical wave tank, an improved representation of the instantaneous velocity field associated with the instantaneous location of the free surface, making an accurate estimation of the wave load of

highly nonlinear and breaking waves possible at a reasonable computational cost. Further, a slamming model is presented, where the slamming load comes from the rapid change of added mass momentum, giving rise to an additional slamming term in the load time series.

In this paper, two cases are investigated to present the method and examine its capabilities and limitations:

- In the first case, the hydrodynamic load acting on a mono-pile with a diameter $D = 0.7$ m is estimated due to a steep incident regular wave with wave heights $H = 1.2$ m and with wave periods $T = 4.0$ s where the bottom is horizontal (const. water depth $h = 4.76$ m).
- The second case investigates the same mono-pile in slightly steeper wave environment, where the incident wave heights are larger, $H = 1.3$ m but with the same wave periods as that in the first case. The mono-pile is placed with its central axis at the top of the slope which forces the wave to break during passing the top of the slope.

The open-source fully nonlinear potential flow model REEF3D::FNPF is employed for the wave propagation calculations, which is already successfully applied for simulation of three-hours finite water depth irregular sea states [12–14]. The results of both cases are compared against model test data.

IMPLEMENTATION
Nonlinear Wave Tank with σ-grid

As mentioned in the abstract, the governing equation for the fully nonlinear potential flow model in REEF3D::FNPF is the Laplace equation:

$$\frac{\partial^2 \Phi}{\partial x^2} + \frac{\partial^2 \Phi}{\partial z^2} = 0. \tag{1}$$

Boundary conditions are required in order to find the unique solution of the velocity potential Φ from this elliptic equation, especially at the free surface and at the seabed. These are the kinematic and dynamic boundary conditions which must be fulfilled at all times and are prescribed as follows:

$$\frac{\partial \eta}{\partial t} = -\frac{\partial \eta}{\partial x}\frac{\partial \widetilde{\Phi}}{\partial x} + \widetilde{w}\left(1 + \left(\frac{\partial \eta}{\partial x}\right)^2\right) \tag{2}$$

$$\frac{\partial \widetilde{\Phi}}{\partial t} = -\frac{1}{2}\left[\left(\frac{\partial \widetilde{\Phi}}{\partial x}\right)^2 - \widetilde{w}^2\left(1 + \left(\frac{\partial \eta}{\partial x}\right)^2\right)\right] - g\eta \tag{3}$$

where η is the free surface elevation, $\widetilde{\Phi} = \Phi(\mathbf{x}, \eta, t)$ is the velocity potential at the free surface, $\mathbf{x} = (x, y)$ represents the location
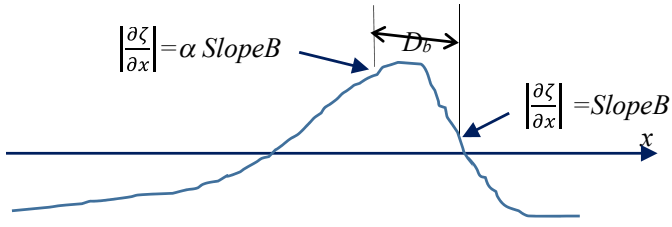
FIGURE 1: Schematic sketch for breaking-wave model definition from [7]

at the horizontal plane and $\widetilde{w}$ is the vertical velocity at the free surface.

The empirical breaking-wave model presented by [7] is implemented in REEF3D::FNPF. Both free surface conditions (2) and (3) are modified and extended by one extra element which mimics a spilling breaker and models energy dissipation similar to turbulent viscosity.

The additional elements of the free surface conditions is defined as:

$$\frac{\partial \eta}{\partial t} = \ldots + \nu_B(x,t)\left(\frac{\partial^2 \eta}{\partial x^2}\right)$$
$$\frac{\partial \widetilde{\Phi}}{\partial t} = \ldots + \nu_B(x,t)\left(\frac{\partial^2 \widetilde{\phi}}{\partial x^2}\right) \quad (4)$$

where the so called wave-breaking turbulent viscosity $\nu_B(x,t)$ is given by

$$\nu_B(x,t) = \begin{cases} \nu_{B0}, & x \in D_b \\ 0, & \text{otherwise.} \end{cases} \quad (5)$$

D_b is the region where the dissipation is applied. Its location is defined by two parameters α and $SlopeB$ where $SlopeB = \partial \eta / \partial x$ is the front steepness of a wave and its value defines the limit when a wave will be identified as breaking in the potential solver and the value of α define the length of the damping zone (D_b) upwave (Figure 1).

The bottom boundary condition represents an impervious solid boundary:

$$\frac{\partial \Phi}{\partial z} + \frac{\partial h}{\partial x}\frac{\partial \Phi}{\partial x} = 0, \ z = -h. \quad (6)$$

where $h = h(\mathbf{x})$ is the water depth measured from the still water level to the seabed.

The Laplace equation with the boundary conditions is solved with a finite difference method on a σ-coordinate system. A σ-coordinate system deforms with the free surface and is also flexible in the handling of irregular boundaries. The relationship between a Cartesian grid and a σ-coordinate is as follows:

$$\sigma = \frac{z + h(\mathbf{x})}{\eta(\mathbf{x},t) + h(\mathbf{x})}. \quad (7)$$

The vertical grid stretching is defined with the help of the sinh function:

$$\tilde{\sigma} = 1 - \frac{\sinh(\delta(\sigma - 1))}{\sinh(-\delta)} \quad (8)$$

where σ is the uniform σ-coordinates, δ is the stretching factor and $\tilde{\sigma}$ is the new σ-coordinates. $\tilde{\sigma}$ will be referred as σ further in this paper. This stretching method is used in the simulations with uniform horizontal grid spacing. The grid is generated by REEF3D at the start of the simulation.

Once the velocity potential Φ is obtained in the σ-domain, the velocities can be calculated as follows:

$$u(\mathbf{x},z) = \frac{\partial \Phi(\mathbf{x},z)}{\partial x} = \frac{\partial \Phi(\mathbf{x},\sigma)}{\partial x} + \frac{\partial \sigma}{\partial x}\frac{\partial \Phi(\mathbf{x},\sigma)}{\partial \sigma}, \quad (9)$$
$$w(\mathbf{x},z) = \frac{\partial \Phi(\mathbf{x},z)}{\partial z} = \frac{\partial \sigma}{\partial z}\frac{\partial \Phi(\mathbf{x},\sigma)}{\partial \sigma}. \quad (10)$$

Wave generation is handled using the relaxation method [15], with the relaxation function presented by Jacobsen et al. (2012):

$$\Gamma(x_R) = 1 - \frac{e^{(1-x_R)^{3.5}} - 1}{e} \quad (11)$$

where $\Gamma(x)$ is the relaxation function and $x_R \in [0,1]$ is the length scale along the relaxation zone (Figure 3). This relaxation function modifies only the free surface boundary conditions of the Laplace equation, the location of the free surface η and the value of the velocity potential on the free surface $\widetilde{\Phi}$. The solution of the previous time step is mixed with the prescribed solution in the relaxation zones with the help of the relaxation function. This ensures a smooth transition of the predefined solution with current numerical solution. If the predefined solution is corresponding to the still water solution, the relaxation function absorbs any waves and their reflection from the end of the wave tank, traveling backwards from the relaxation zone. This prevents wave reflection and simulates a beach. The newly presented Steady Surface Gravity Wave (SSGW) method by Clemand et al. [16], which is implemented in REEF3D::FNPF, is used to prescribe

the free surface location and potential for regular wave generation. The main advantage with the SSGW method compared to other methods is that the method allows the arbitrary precision computation of waves in arbitrary depth.

ALE Kinematic Description

The nomenclature and description of the laws of motion used in this article follows the Arbitrary Lagrangian-Eulerian (ALE) methods presented by [17]. The instantaneous material coordinate of a water particle is symbolised by $\vec{X}$ which links to a fixed coordinate (Eulerian) $\vec{x}$ by the law of motion:

$$\vec{x} = x(\vec{X}, t) \quad \text{at} \quad t = t \tag{12}$$

and describes the location of the water particle at a given time in a fixed Eulerian frame.

The material velocity $\vec{v}$ can be expressed as local derivative of x:

$$\vec{v}(\vec{X}, t) = \left. \frac{\partial x}{\partial t} \right|_{\vec{x}} \tag{13}$$

where $|_{\vec{x}}$ denotes the material coordinate $\vec{X}$ is fixed at $\vec{x}$. In a Lagrangian system the motion of the material is described in a moving frame, where the velocity of the system is equal to the material velocity. In an Eulerian system, the material motion is followed in a time independent framework. In the ALE description of motion with the ALE coordinate $\vec{\chi}$, the coordinate system moves with a mesh velocity $\vec{\hat{v}}$ which does not equal to the material velocity $\vec{v}$.

The fundamental ALE equation describes the relationship between the material or total time derivatives and the referential or local time derivatives. The transformation from the material to an Euler system is known as the Reynolds transport theorem, which can written in differential form as:

$$\frac{df}{dt} = \frac{\partial f}{\partial t} + \vec{v} \cdot \nabla f$$

and with the above introduced ALE nomenclature as:

$$\left. \frac{\partial f}{\partial t} \right|_{\vec{X}} = \left. \frac{\partial f}{\partial t} \right|_{\vec{x}} + \vec{v} \cdot \frac{\partial f}{\partial \vec{x}}. \tag{14}$$

Similarly, the transformation from the material to an ALE system is:

$$\left. \frac{\partial f}{\partial t} \right|_{\vec{X}} = \left. \frac{\partial f}{\partial t} \right|_{\vec{\chi}} + \vec{c} \cdot \frac{\partial f}{\partial \vec{x}} \tag{15}$$

where $\vec{c} = \vec{v} - \vec{\hat{v}}$ defines the the relative velocity between the material and the mesh velocity. Using Eq. (15), the total derivative of any variable f from an ALE representation can be defined. For example the material acceleration ($\vec{a} = d\vec{v}/dt$) can be expressed in an ALE system as:

$$\vec{a} = \left. \frac{\partial \vec{v}}{\partial t} \right|_{\vec{\chi}} + \vec{c} \cdot \frac{\partial \vec{v}}{\partial \vec{x}} \tag{16}$$

where the convective derivative ($\nabla \vec{v} = \frac{\partial \vec{v}}{\partial \vec{x}}$) is usually calculated in the Eulerian system ($\vec{x}$).

Morison Equation defined over an ALE Kinematic Description

REEF3D::FNPF calculates the velocity potential over a $\vec{\sigma}$-grid, where the mesh follows the free surface elevation at the top and is fixed at the bottom, resulting in the mesh being deformed by the free surface. Such a grid can be treated as an ALE system. The derivatives of the velocity potential, meaning the velocity components, can also be obtained in the ALE system. In this section, direct estimation of the total acceleration on the $\vec{\sigma}$-grid using the relationship for the total acceleration shown above is presented for a two-dimensional case as an example. The definition of the $\vec{\sigma}$ coordinates in Eq. (7) defines the relationship between the Eulerian and the ALE coordinates :

$$\vec{\sigma} = \begin{bmatrix} \xi \\ \sigma \end{bmatrix} = \begin{bmatrix} x \\ \dfrac{z(t)+h}{h+\eta(x,t)} \end{bmatrix} \tag{17}$$

and vice versa

$$\vec{x} = \begin{bmatrix} x \\ z \end{bmatrix} = \begin{bmatrix} x \\ \sigma(h+\eta(x,t)) - h \end{bmatrix} \tag{18}$$

where x and z are the locations of the $\vec{\sigma}$-grid points. Based on this relationship, the convective velocity can be defined from $\vec{c} = \vec{v} - \vec{\hat{v}}$ as:

$$\vec{c} = \begin{bmatrix} c_x \\ c_z \end{bmatrix} = \begin{bmatrix} u \\ w - \sigma \left. \dfrac{\partial \eta(x,t)}{\partial t} \right|_{\vec{x}} \end{bmatrix} \tag{19}$$

where u is the horizontal fluid velocity and w the vertical fluid velocity component. The vertical component of the convective velocity can be estimated directly from the local time derivative of the free surface location, which is already known from the kinematic free surface condition in Eq. (2). In order to apply Eq. (16), it is necessary to define the convective derivative

Copyright © 2021 by ASME

$(\nabla \vec{v} = \partial \vec{v}/\partial \vec{x})$ using the σ-grid framework. The derivatives can be estimated by the means of the chain rule. The modified Morison equation uses the horizontal material acceleration, which can be estimated in an Eulerian system according to Eq. (14) for the two-dimensional case as:

$$a_x = \left.\frac{\partial u}{\partial t}\right|_{\vec{x}} + \vec{v} \cdot \frac{\partial u}{\partial \vec{x}} = \left.\frac{\partial u}{\partial t}\right|_{\vec{x}} + u\frac{\partial u}{\partial x} + w\frac{\partial u}{\partial z} \qquad (20)$$

and in the ALE system according to Eq. (16) as:

$$a_x = \left.\frac{\partial u}{\partial t}\right|_{\vec{\sigma}} + u\left(\frac{\partial u}{\partial \xi} + \frac{\partial u}{\partial \sigma}\frac{\partial \sigma}{\partial x}\right) + \left(w - \sigma\left.\frac{\partial \eta(x,t)}{\partial t}\right|_{\vec{x}}\right)\frac{\partial u}{\partial \sigma}\frac{\partial \sigma}{\partial z} \qquad (21)$$

where all terms are known or defined in the $\vec{\sigma}$ system. The incremental horizontal force acting on a strip is defined according to the Morison equation [18] as:

$$\Delta F_x == C_M a_x \rho A_{xy} \Delta z + C_D u|u|\frac{1}{2}\rho B_p \Delta z \qquad (22)$$

where C_M is the inertia coefficient, $\Delta V = A_{xy}\Delta z$ is the volume of the strip (with the cross sectional area A_{xy}), C_D is drag coefficient, ΔA is the projection area, with the section breadth B_p and strip thickness Δz. By integration over the wetted portion of an object, the global horizontal force is defined as:

$$F_x = \lim_{\Delta z \to 0} \sum \Delta F_x = \int_0^{\eta(x,t)} C_M a_x \rho A_{xy} dz + \int_0^{\eta(x,t)} C_D u|u|\frac{1}{2}\rho B_p dz \qquad (23)$$

which can be estimated in the $\vec{\sigma}$ coordinate system as:

$$F_x = \rho\left(h + \eta(x,t)\right)\left[\int_0^1 C_M a_x A_{xy} d\sigma + \int_0^1 C_D u|u|\frac{1}{2}B_p d\sigma\right]. \qquad (24)$$

The main advantages of the using the Morison equation with ALE strips are:

- As all strips are always under water, the wetted volume need not be explicitly calculated depending on the location of the free surface as in the case of Eulerian strips
- Forces can be directly calculated from the numerical results without any interpolation to a fixed Eulerian frame.

Slamming Load Model over an ALE Kinematic Description

In the paper [19] the original method is described by Nestegård et al. over an Eulerian framework as: "The vertical cylinder is divided into a number of sections and the distributed pressure load on the cylinder is represented as the sum of loads on each two-dimensional section in a strip wise manner. The measured wave elevation close to the cylinder gives the time instant when a section is "hit" by the wave and starts to penetrate the sloping water surface." The principle of the method is explained in Figure 2. The dominating contribution to the slamming load when the wave hits the cylinder is the rate of change of added mass momentum. Assuming constant horizontal velocity, this rate of change can be represented as the rate of change of added mass of a circular cylinder with respect to penetration distance s under a drop test with constant vertical velocity. Experimental values for this rate are available and have been represented by an analytical formula [20]. Defining the slamming or impact coefficient:

$$C_S = \frac{2}{\rho D}\frac{dA^{2D}}{ds} \qquad (25)$$

where D is the diameter of the cylinder, ρ is the water density and A^{2D} is the high-frequency limit of the added mass for a cylindrical section (two-dimensional) as a function of submergence $s = s(t)$ relative to the wave surface. the impact force can be written in a form similar to the viscous drag force:

$$f(z,t) = \frac{1}{2}\rho C_S D u^2 \qquad (26)$$

where u is the relative horizontal velocity between wave surface and cylinder. An analytic fit to the experiments [20] defines the impact coefficient as:

$$C_S(s) = 5.15\left[\frac{D}{D+19s} + \frac{0.107s}{D}\right]. \qquad (27)$$

In the original method, the value of $s(z)$ is estimated from the location of the free surface $\eta(x)$ for each fixed strip and the forces
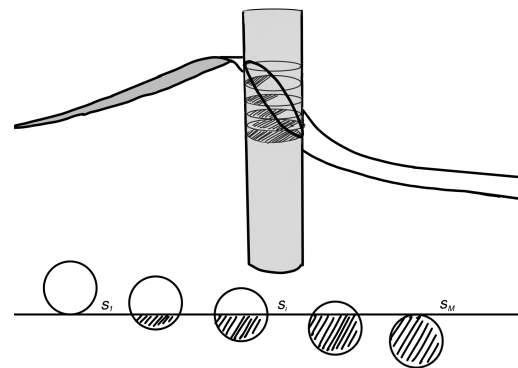

FIGURE 2: Concept of the slamming force estimation

Copyright © 2021 by ASME

is calculated based on (27) and (26) and the total slamming force is estimated by the integration of these values over a fixed z interval:

$$F_S(t) = \int_{z_1}^{z_N} f(z,t)\mathrm{d}z = \sum_{i=1}^{N} \frac{1}{2}\rho C_S(s(z_i))Du(z_i)^2 \Delta z_i \qquad (28)$$

where N is the number of the strips. The estimation of the value of $s(z_i)$ is not trivial and therefore, an alternative way to define the total forces is applied. Instead of estimating $s(z)$ at fixed vertical location, the horizontal location is fixed for a constant value of $s(x_i)$, and the free surface location and the horizontal velocity at these positions is identified. The force at the strips are calculated the same way according (26), however the integration limit is now time dependent similar to the ALE formulation of the Morison equation.

$$F_S(t) = \int_{z(s_1)}^{z(s_M)} f(z,t)\mathrm{d}z = \int_{z(s_1)}^{z(s_M)} \frac{1}{2}\rho C_S(s(x_i))Du(x_i)\,|u(x_i)|\,\mathrm{d}z. \qquad (29)$$

The square of the horizontal velocity is also exchanged to $u(x_i)\,|u(x_i)|$.

In this simplified method, constant horizontal velocity for a given time instant is assumed and each strip is treated independently. The strip force depends only on instantaneous horizontal velocity at the free surface and the penetration distance. Therefore, the original formulation and the new expression yields the same result. The advantage of this method is similar to the above presented Morison force estimation over the ALE formulation. Only the wetted sections are included in the force estimation and it is not necessary to identify the sections that are dry and wet explicitly.

Experimental Setup

As mentioned in the introduction, two experiments are used to validate the presented method. Both experiments are carried out at the Large Wave Flume (GWK), Hannover, Germany by Mo et al. , [21] and Irschik et al., [22]. The wave flume in the experiments is 309 m long, 5 m wide.

In the first experiment, a cylinder of diameter $D = 0.7$ m is placed 111 m from the wavemaker, the water depth $h = 4.76$ m and strain gages are placed at the top and bottom of the cylinder to measure wave forces. Wave gages are placed at several locations around the cylinder to measure the time histories of the free surface elevation. The free surface elevation is measured only in the appearance of the cylinder therefore only the recorded time series of the wave gage at the side wall of the flume is used for the comparison. The published measured time series are all normalised with the wave height H and with the wave period T. The experimental time series are presented without normalisation in
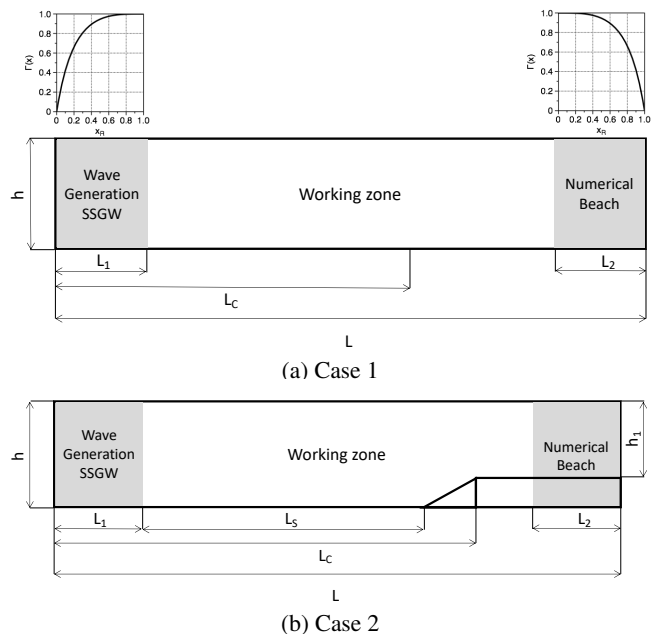

FIGURE 3: Numerical setup

this paper, using the defined wave height $H = 1.2$ m and wave period $T = 4.0$ s [21]. In the second experiment, a 23 m long 1:10 slope reaching a height of 2.3 m is placed at 179.0 m from the wavemaker. A flat bed extends from the end of slope with a height of 2.3 m. A vertical cylinder of diameter $D = 0.7$ m is placed with its central axis at the top of the slope.

Numerical Setup

The numerical simulations follows the experimental setup. The numerical domain for both cases is shown in Figure 3 and the parameters can be taken from Table 1, where L_C is the location of the cylinder.

As mentioned earlier, the SSGW method is used to generate the regular wave in REEF3D::FNPF. The input values for the SSGW method are shown in Table 2, which yield regular waves with a wave period $T = 4.00$ s.

The number and distribution of vertical grids has a significant effect on wave dispersion in a numerical simulation using the Laplace equations [23]. Pakozdi et al. [24] have shown that a minimum of 35 grids per wavelength is necessary ($dx = \lambda/35$)

TABLE 1: Numerical setup

	L [m]	L_1 [m]	L_2 [m]	h [m]	L_C [m]	L_S [m]	h_1 [m]
Case 1	201.00	22.58	45.16	4.76	111.00		
Case 2	301.00	21.49	42.98	3.8	201.00	179.00	1.5

TABLE 2: Input of SSGW

	H [m]	λ [m]	h [m]	TOL	N
Case 1	1.20	22.58	4.76	10^{-15}	1024
Case 2	1.30	21.49	3.8	10^{-15}	1024

in the model for the satisfactory representation of regular waves and a method to identify the optimum distribution for a given wave period. Using the wave propagation velocity $C_{phase} = \lambda/T$ with this grid size, the largest possible time step for the numerical simulation is $dt = dx/C_{phase}$.

Case 1: In the simulation 45 vertical grid points per wavelength are used ($dx = 0.5$ m) with a 25% reduced time step $dt = 0.75 dx/C_{phase} = 0.065$ s. The optimal vertical grid distribution is identified for a number of the vertical grids 15, for the given water depth and for the given wave period which corresponds to a stretching factor $\delta = 1.35$.

Case 2: After the identification of the optimal vertical distribution for the water depths 3.8 m and 1.5 m it has been identified that same stretching factor can be used for this case. A grid sensitivity and time step sensitivity studies show that it is necessary to use significantly higher horizontal grid and time resolution for this case compared to the one with a horizontal bottom, in order to correctly capture the wave shoaling process over the slope. The time step study shows that it is necessary to reduce more than 80% of the time step relative to the above presented largest possible time step $dt = 0.19 dx/C_{phase}$ where the phase velocity is defined for the 3.8 m water depth. Only the results of the horizontal grid resolution study are shown in this paper in the next section.

RESULTS AND DISCUSSION

A post-processing procedure to determine the wave forces on a cylinder is developed based on the methods presented in the previous sections.

Horizontal Bottom

In this section, a regular wave is chosen to demonstrate the utility of the method and validate the results of the procedure by calculating the hydrodynamic loads on the structure and comparing them to the measured global forces.

Applying (21) to the σ-grid, the total horizontal acceleration is defined at all grid points. With the help of a spline function, these values, a_x and u are interpolated to the location of interest: $\xi = 111.00$ m for all σ positions. This procedure is followed for each numerical time step to obtain time series of the instantaneous z-coordinates, the total horizontal acceleration a_x and the
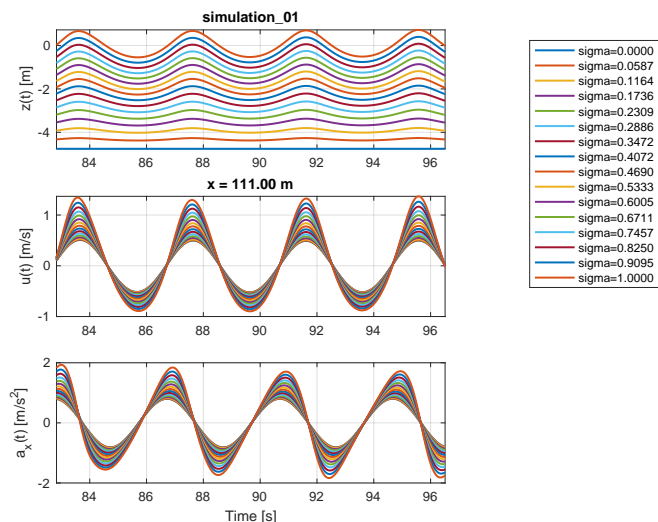
FIGURE 4: The estimated time series at $x = 111.00$ m

horizontal velocity at the predefined σ values as shown in Figure 4. The free surface location at $\sigma = 1.0$ and the bottom at $\sigma = 0.0$ are seen in the upper diagram. The increase in the magnitude of the parameters with increasing vertical location is also seen. The time series of the horizontal velocity and acceleration are smooth, as they continuously include the velocity and acceleration at the free surface ($\sigma = 1.0$).

The forces are calculated using (24) for every time step. The integration is done with help of the Matlab function `mmpint` [25], which integrates a curve based on its cubic spline representation. The integration is split into the inertial forces and moments with the unit inertial coefficient C_M and the viscous forces and moments with the unit drag coefficient C_D. This makes a sensitivity study of the coefficients straightforward.

The numerically estimated hydrodynamic loads, the measured global force as well as the free surface elevations are presented in Figure 5. The upper diagram shows a good agreement
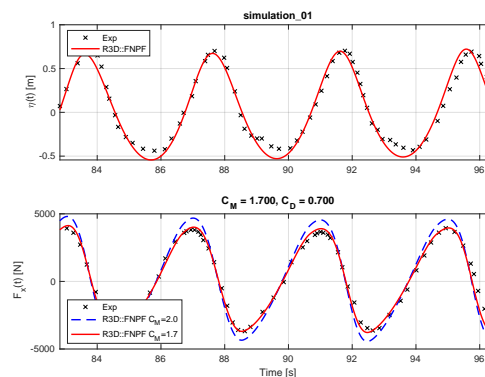
FIGURE 5: Comparison of the numerical and measured free surface elevation and the horizontal force for regular waves with horizontal bottom
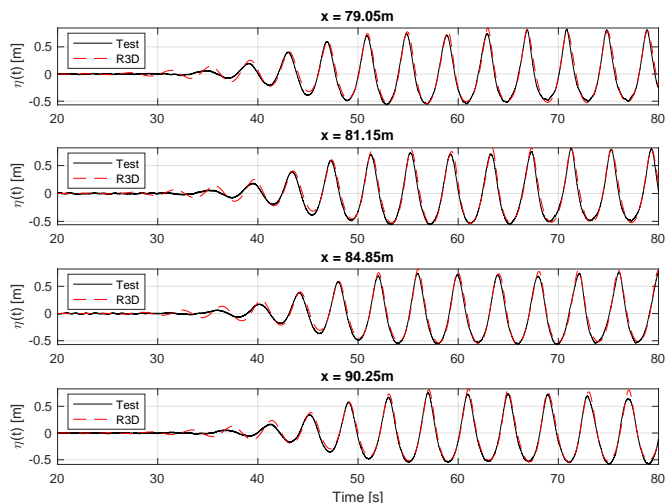
FIGURE 6: Comparison of the numerical and measured free surface elevation over horizontal bottom

between the crest shapes and the crest heights. The differences at the troughs might be explained by the nonlinear wave structure interaction which is not accounted for in the simulation. A good agreement between the measured and estimated force time series with the chosen inertial coefficient and drag coefficient is also seen. The inertial force and moment are calculated using inertial coefficient $C_M = 1.70$ and drag coefficient $C_D = 0.7$. These values correspond to suggestions by DNV-GL [26], but are less than those proposed by Irschick [22], $C_M = 2.00$.

Bottom with Slope

In the experiment, the regular waves propagates over 179 m from the wavemaker up to the slope. This phase is very similar to the case presented above. The comparison of the measured and numerically estimated time series of the free surface elevations is presented in Figure 6 for six different locations. The comparison of the time series of the measured and calculated free surface elevation shows a good agreement. At the beginning, one can see larger differences due to the ramp function. REEF3D::FNPF has an inbuilt linear ramp function and due the lack of measured wavemaker signal it was not possible to estimate original shape and duration of the ramp function used in the experiments. No significant change in the numerical results are observed in this phase of simulation in the earlier mentioned sensitivity studies and only one result is presented here.

In the second phase, when the waves pass over the slope, wave shoaling and wave breaking on the top of the slope or slightly downstream [4] is observed. The correct simulation of such extreme breaking waves is not possible using potential theory based models. However, it was shown in Pakozdi [14] that it is possible to correctly simulate the waves over a slope with

REEF3D::FNPF up to wave breaking. The free surface elevations are measured at several location along the slope and at the location of the cylinder, but the water particle velocity is not recorded at the location of the cylinder. With the help of the definition of wave breaking the horizontal water particle velocity is larger than the wave propagation velocity, it is possible to estimate the horizontal water particle velocity just before the wave breaking. The largest horizontal velocity in shallow water is defined by the water depth:

$$C_{max} = \sqrt{gh} = \sqrt{9.81\,\text{m/s}^2 1.5\,\text{m}} = 3.84\,\text{m/s} \qquad (30)$$

where g is the gravity acceleration. It is expected that the value of the horizontal water particle velocity is close to this value.

In this paper, four simulations are presented and the main numerical parameters are listed in Table 3. The comparison of the first two simulations shows the effect of the wave breaking turbulent viscosity in Figure 7, 8 and 9. The wave crest height increases first at the location of the cylinder at $x = 201.00$ m and about 10% downstream of the cylinder according to the free surface elevation time series. However, the wave becomes steeper and the horizontal velocity larger when the wave reaches the end of the slope according to Figure 8. The blue, red and white points on the free surface nodes show the status of the breaking model. Between the white points, where the other nodes are red, wave breaking is identified and the free surface conditions are modified according to (4), but not at the blue points. The change of the wave kinematics can also be observed by the time series of the fluid at the location of the cylinder. The horizontal velocity and acceleration of the water particles increase significantly, from 2.6 m/s to 3.7 m/s and from 8.0 m/s² to 12.0 m/s² in Figure 9. Some unphysical peaks are seen in the load signal, arising from the numerical treatment of wave breaking. When the wave breaking algorithm in the numerical simulation is activated, it reduces the wave elevation and the fluid velocity to account for the energy dissipation due to wave breaking. This dissipation due to wave breaking causes a sudden change in the local horizontal fluid acceleration, which leads to the peaks calculated in the global load curves. In these simulations, the peaks are of a reasonable magnitude and are interpreted as an unphysical artefact of wave breaking in a Laplace equations-based model and are removed with the help of a low pass filter. These effects are not shown in this paper.

Increasing the horizontal grid resolution only has a small effect on the wave kinematics as shown in Figure 10. The wave steepness and the horizontal water particle velocity are almost the same. When the free surface elevation and the estimated forces are compared with all four simulations and with the experimental time series where possible in Figure 11, one can see the influence of the wave breaking turbulent viscosity ν not only on the wave kinematics but also on the estimated forces. The up-

TABLE 3: Sensitivity study

Sim. Nr.:	N_x	dx [m]	N	dt [s]	CFL	v	$SlopeB$	α	Nr. of Proc.	CPU Time [s]
00	752	0.4	11280	0.020	0.19	1.86	1.25	0.1	4	310
01	752	0.4	11280	0.020	0.19	0.1	1.25	0.7	4	310
02	1505	0.2	22575	0.010	0.19	0.1	1.25	0.7	6	860
03	3010	0.1	45150	0.005	0.19	0.1	1.25	0.7	12	2817

per left hand side diagram compares the free surface elevations at the location of the cylinder. The significant effect comes from the wave breaking viscosity, the finer grid only slightly increases the wave crest height. All NWT simulations overestimate the crest height except the first simulation, which is a clear hint that the value of viscosity is too large. The upper right hand side diagram shows the comparison of the Morison forces. The trend is similar to the left diagram, the significant effect comes from the wave breaking viscosity. This is not true for the lower left hand side diagram, where the slamming force time series are compared. The reduction of the value of v triggers a much larger slamming force, but the horizontal grid refinement has a larger effect than before. This is explained by the larger horizontal velocity at the free surface and the higher wave crest height. The last diagram, on the lower right hand side, the comparison of the total forces with the measurement is shown. Because of the dynamical amplification of the experimental equipment the experimental data is filtered and modified by the Empirical Mode Decomposition (EMD) [27]. Therefore, the experimental data cannot be treated with absolute confidence. However, the REEF3D::CFD simulation [4], shows the same maximum value of the forces as in the experiment. The potential theory-based simulation yields a similar magnitude. A closer look at the time series of the potential theory-based method shows that this method is not able to reproduce the sudden increase of the force during the impact as it is observed in the experiment. The reason for this slower change can lie on the nature of the solver. The method is based on a one-phase fluid simulation where the steepness of the free surface elevation is limited, unlike a two-phase REEF3D::CFD solver where an upright free surface position can also be represented as it was shown in [4]. Therefore, a steeper wave propagates faster and causes a larger rate of the change of the wetted area on the mono-pile. The cost of this flexibility is the significantly larger CPU cost. The REEF3D::CFD simulation uses 15.12 million cells [4], while in REEF3D::FNPF it is only 45,150.

CONCLUSION

A novel approach to evaluate hydrodynamic loads on a cylinder using a combination of strip theory and Morison equation with wave kinematics from a nonlinear NWT is presented.

Further, a slamming load model is modified to be used with wave kinematics from a nonlinear NWT. The method is used to evaluate the hydrodynamic loads on a cylinder in regular waves over a horizontal and a sloping bottom. The calculated free surface elevation and the hydrodynamic loads are seen to be in good agreement with the measurements and imply that the wave kinematics are well represented. Some unphysical peaks are seen in the load signal which arise from the numerical treatment of wave breaking and the use of a low-pass filter on the numerical signal is justified.

The results are promising, but limitations to the presented method are also seen. The potential theory-based method is inherently not capable of accurately accounting for extremely steep or breaking waves. This is only possible with a two-phase CFD solver. The presented method might be not sufficiently conservative for the estimation of the high frequency resonance like structure response due to a wave slamming. However, this method can be used in the early phase of the design to produce a sufficiently good estimate of the hydrodynamic loads in a fast and economical manner. The method can be also used as a screening tool to identify critical events of run-up or slamming for further coupled simulation where the far field solution for input into the CFD simulation is defined by the NWT.

ACKNOWLEDGMENT

REFERENCES

[1] Frandsen, S., Tarp-Johansen, N. J., Hansen, E. A., Høgedal, M., Ibsen, L. B., and Jensen, L., 2006. "Offshore wind turbine design: addressing uncertainty drivers". In 2006 European Wind Energy Conference and Exhibition, European Wind Energy Association (EWEA).

[2] Pakozdi, C., Ostman, A., Ji, G., Stansberg, C. T., Reum, O., Ovrebo, S., Vestbostad, T., Sorvaag, C., and Ersland,

J., 2016. "Estimation of wave loads due to green water events in 10000-year conditions on a tlp deck structure". In Proceedings of the ASME 2016 35th International Conference on Ocean, Offshore and Arctic Engineering, no. OMAE2020-18298, ASME.

[3] Pakozdi, C., Östman, A., Abrahamsen, B., and Økland, O.D., Vestbøstad, T.M., L. G. . S. C., 2017. "New combined cfd and model testing technique for identification of wave impact loads on a semisubmersible". In Proceedings of the ASME 2016 35th International Conference on Ocean, Offshore and Arctic Engineering, no. OMAE2017-62643, ASME.

[4] Kamath, A., Chella, M. A., Bihs, H., and Arntsen, Ø. A., 2016. "Breaking wave interaction with a vertical cylinder and the effect of breaker location". *Ocean Engineering, 128*, pp. 105 – 115.

[5] Chella, M. A., Bihs, H., and Myrhaug, D., 2019. "Wave impact pressure and kinematics due to breaking wave impingement on a monopile". *Journal of Fluids and Structures, 86*, pp. 94–123.

[6] Pakozdi, C., Östman, A., Stansberg, C., Peric, M., Lu, H., and Baarholm, R., 2015. "Estimation of wave in deck load using cfd validated against model test data". In The Twenty-fifth International Ocean and Polar Engineering Conference, no. ISOPE-I-15-586, ISOPE.

[7] Baquet, A., Kim, J., and Huang, Z., 2017. "Numerical modeling using CFD and potential wave theory for three-hour nonlinear irregular wave simulations". In ASME 2017 36th OMAE, no. OMAE2017-61090.

[8] Huang, Z., and Guo, Q., 2017. "Semi-empirical crest distributions of long-crest nonlinear waves of three-hour duration". In Proceedings of the ASME 2017 36th International Conference on Ocean, Offshore and Arctic Engineering, no. OMAE2017-61226, ASME.

[9] Sharma, J. N., and Dean, R. G., 1981. "Second-order directional seas and associated wave forces". pp. 129–140.

[10] Marthinsen, T., and Winterstein, S., 1992. "On the skewness of random surface waves". *Proceedings of the Second International Offshore and Polar Engineering Conference (ISOPE), III*, pp. 472–478.

[11] Bachynski, E. E., Kristiansen, T., and Thys, M., 2017. "Experimental and numerical investigations of monopile ringing in irregular finite-depth water waves". pp. 154–170.

[12] Bihs, H., Wang, W., Pakozdi, C., and Kamath, A., 2020. "REEF3D::FNPF—A flexible fully nonlinear potential flow solver". *Journal of Offshore Mechanics and Arctic Engineering, 142*(4).

[13] Wang, W., Kamath, A., Martin, T., Pakozdi, C., and Bihs, H., 2020. "A comparison of different wave modelling techniques in an open-source hydrodynamic framework". *Journal of Marine Science and Engineering, 8*(7), p. 526.

[14] Pakozdi, C., Fouques, S., Thys, M., Kamth, A., Wang, W., Dadmarzi, F. H., Bachynski, E., and Bihs, H., 2020. "Validation of numerical wave tank simulations using reef3d with jonswap spectra in intermediate water depth". In Proceedings of the ASME 2020 39th International Conference on Ocean, Offshore and Arctic Engineering, no. OMAE2020-18298.

[15] Engsig-Karup, A. P., Hesthaven, J. S., Bingham, H. B., and Warburton, T., 2008. "DG-FEM solution for nonlinear wave-structure interaction using boussinesq-type equations". *Coastal Engineering, 55*(3), pp. 197–208.

[16] Clamond, D., and Dutykh, D., 2018. "Accurate fast computation of steady two-dimensional surface gravity waves in arbitrary depth". *Journal of Fluid Mechanics, 844*, p. 491–518.

[17] Donea, J., Huerta, A., Ponthot, J.-P., and Rodriguez-Ferran, A., 2004. "Arbitrary Lagrangian-Eulerian methods". pp. pp. 413–437.

[18] Morison, J. R., Johnson, J. W., and Schaaf, S. A., 1950. "The force exerted by surface waves on piles". pp. 149–154.

[19] Nestegård, A., Kalleklev, A. J., Hagatun, K., Lin Wu, Y., Haver, S., and Lehn, E., 2004. "Resonant vibrations of riser guide tubes due to wave impact". In The Twenty-third International Ocean and Polar Engineering Conference, no. OMAE2004-51545, ASME.

[20] Campbell, I., and Weynberg, P., 1980. Measurement of parameters affecting slamming. techreport Rep. No. 440, Southampton University: Wolfson Unit for Marine Technology. Technology Reports Centre No. OT-R-8042.

[21] Mo, W., Irschik, K., Oumeraci, H., and Liu, P. L. F., 2007. "A 3D numerical model for computing non-breaking wave forces on slender piles". *J Eng Math, 58*, Aug., pp. 19–30.

[22] Irschik, K., Sparboom, U., and Oumeraci, H., 2002. "Breaking wave characteristics for the loading of a slender pile". In Proceedings of the 28th International Conference on Coastal Engineering.

[23] Engsig-Karup, A. P., Bingham, H. B., and Lindberg, O., 2009. "An efficient flexible-order model for 3D nonlinear water waves". *Journal of computational physics, 228*(6), pp. 2100–2118.

[24] Pakozdi, C., Wang, W., Kamath, A., and Bihs, H., 2019. "Definition of the vertical spacing of a sigma grid based on the constant truncation error". In 10. National Conference on Computational Mechanics, B. Skallerud and H. I. Andersson, eds.

[25] Hanselman, D. C., and Littlefield, B. L., 2011. *Mastering MATLAB*, 1st ed. Prentice Hall Press, USA.

[26] DNV-GL, 2016. Loads and site condition for wind turbines. Tech. Rep. DNVGL-ST-0437, DNV-GL, Nov.

[27] Choi, S. J., Lee, K. H., and Gudmestad, O. T., 2015. "The effect of dynamic amplification due to a structure's vibration on breaking wave impact". *Ocean Eng., 96*, pp. 8–20.
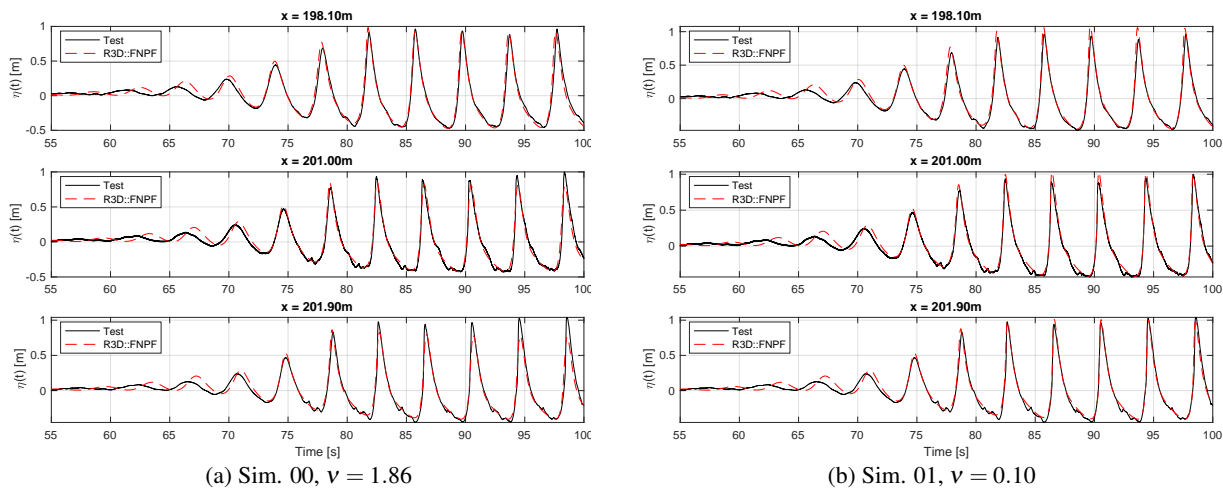
(a) Sim. 00, $\nu = 1.86$ (b) Sim. 01, $\nu = 0.10$

FIGURE 7: Horizontal velocity field during wave crossing the top of the slope

(a) Sim. 00, $\nu = 1.86$ (b) Sim. 01, $\nu = 0.10$
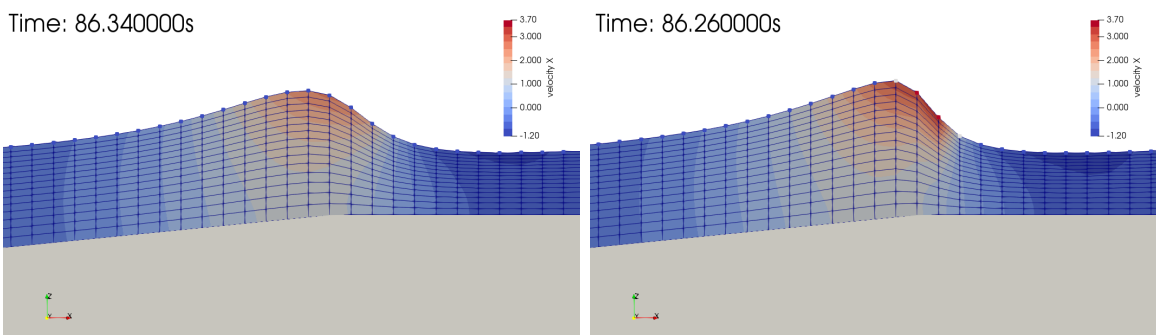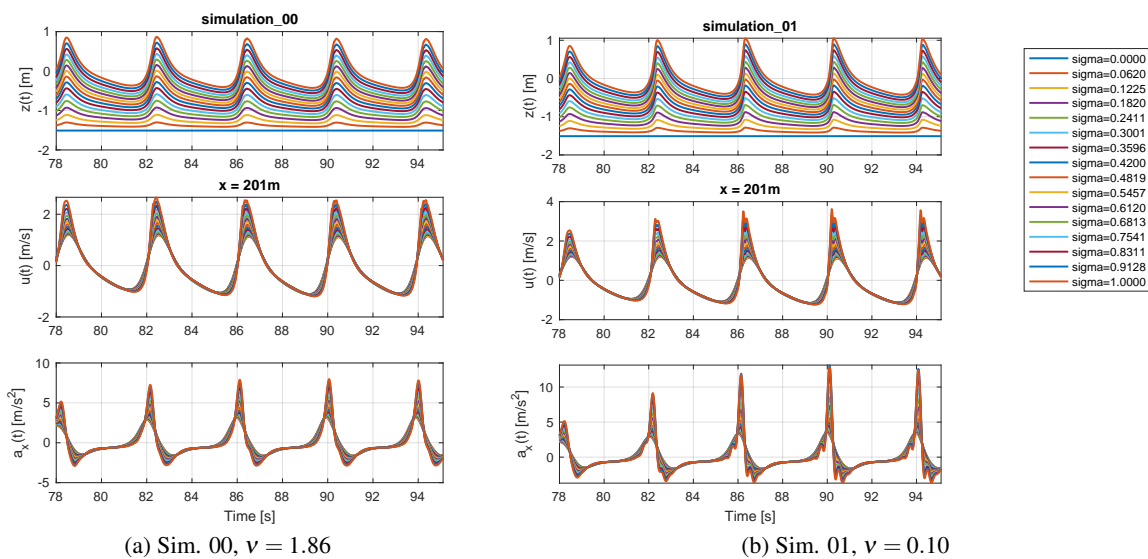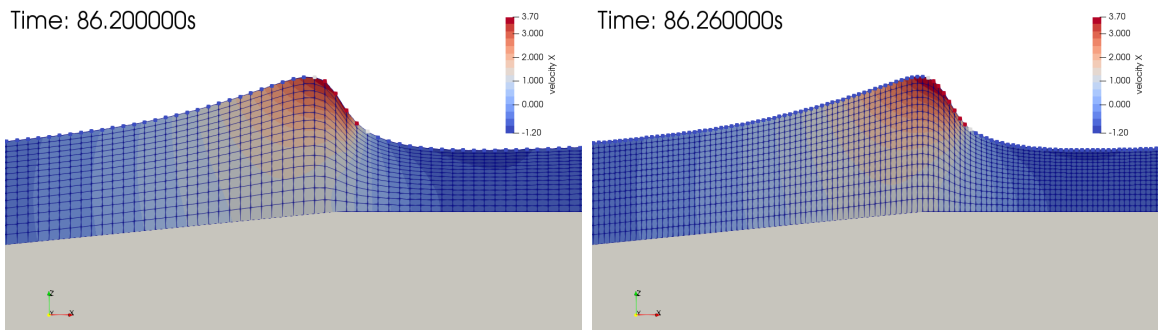
FIGURE 8: Horizontal velocity field during wave crossing the top of the slope

(a) Sim. 00, $\nu = 1.86$ (b) Sim. 01, $\nu = 0.10$

FIGURE 9: Horizontal velocity field during wave crossing the top of the slope

(a) Sim. 02, $dx = 0.010\,\text{m}$

(b) Sim. 03, $dx = 0.005\,\text{m}$

FIGURE 10: Horizontal velocity field during wave crossing the top of the slope
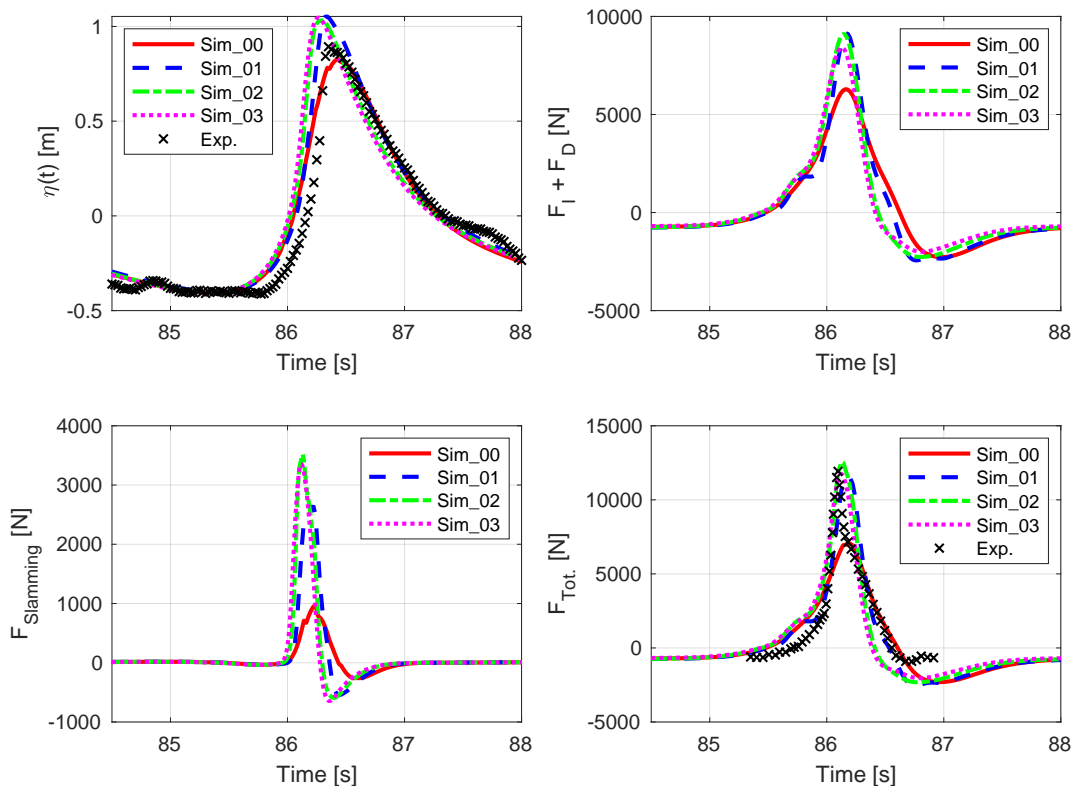

FIGURE 11: Comparison of the numerical results with each other and with measured time series